AIAA JOURNAL
Vol. 48, No. 3, March 2010

Finite Rate Chemistry Large-Eddy Simulation of Self-Ignition in a Supersonic Combustion Ramjet

M. Berglund,* E. Fedina,† C. Fureby,‡ and J. Tegnér†
Swedish Defense Research Agency, SE-147 25 Stockholm, Sweden
and
V. Sabel'nikov§
ONERA, 91761 Palaiseau Cedex, France

DOI: 10.2514/1.43746

In this study, large-eddy simulation is used to analyze supersonic flow, mixing, and combustion in a supersonic combustor equipped with a two-stage fuel injector strut. The present study focuses on mixing, ignition, and flame stabilization and the degree of detail required by the reaction mechanism in the large-eddy simulation model framework. An explicit large-eddy simulation model, using a mixed subgrid model and a partially stirred reactor turbulence-chemistry interaction model, is used in an unstructured finite volume setting. The model, and its components, has been carefully validated in a large number of other studies. To bestow further validation and to provide supplementary information about the physics of mixing and supersonic combustion, experimental data from the National Aerospace Laboratory of Japan's supersonic combustor, equipped with the two-stage strut injector and connected to ONERA's vitiation air heater, are employed. The large-eddy simulation predictions are compared with the experimental centerline wall pressure distribution and the planar laser-induced fluorescence imaging of hydroxide–ion radicals distributions in several cross sections of the combustor, showing excellent qualitative and quantitative agreements. The large-eddy simulation results are furthermore used to elucidate the complicated flow, mixing, and combustion physics imposed by the multi-injector two-stage injector strut. The importance of the combustion chemistry appears weaker than expected but with the one-step mechanism resulting in a too early ignition (caused by local shock wave heating) and a more stable flame, as compared with the more detailed two- and seven-step mechanisms.

Introduction

HIGH-SPEED flight has, for a long time, been of interest to man: both for terrestrial travel and space exploration and transport. Key issues for these types of travel are the vehicle design and the propulsion system and how to integrate the two. In the realm of civilian air transport, the primary goal has been reducing operational cost rather than increasing flight speeds. However, it is still of interest to try to reduce present terrestrial travel times, putting any place on earth within a few hours of flight. Military aircraft design has focused on maneuverability and stealth, features that are difficult to realize in hypersonic flight, whereas hypersonic missiles are under development by many countries. Space travel has, so far, relied on rocket propulsion but, if aerospace planes are to be operationally viable, an air-breathing propulsion system (in which the ambient air is used as an oxidizer) is needed. Because of the provisions of such vehicles, the airframe must be built around the engine, with the engine being the key component. Two types of engines, ramjets [1] and scramjets [2], are preferred for supersonic flight. In a ramjet, the flow is decelerated to subsonic levels before it enters the combustor, allowing an efficient operational regime of $3 < Ma < 5$ (above which the deceleration leads to excessive thermal losses), whereas in a scramjet, the flow through the engine remains supersonic, thus allowing an operational regime of $6 < Ma < 15$. Seamless integration of ramjet and scramjet operations is possible in the same engine [3] by allowing it to sequentially operate as a ramjet, a dual-mode ramjet, a dual-mode scramjet, and a scramjet. Below $Ma \approx 3$, a turbine-based combined cycle (consisting of a bank of gas turbine engines) or a rocket-based combined cycle (with externally or internally integrated rockets) can be used.

Figure 1 presents a generic scramjet, in which fuel is injected into a supersonic airflow. The air is at a sufficiently high temperature and pressure for the fuel to react, and the resulting mixture is expelled from the engine through the nozzle at a higher pressure. The scramjet is composed of four main components: an inlet, an isolator, a combustor, and an exhaust nozzle. The inlet decelerates the flow through a series of oblique shocks, thus increasing its temperature. The isolator is the key component in the seamless transition from ramjet to scramjet mode, separating the combustor from the inlet. During dual-mode ramjet operation, the precombustion shock train continues through the isolator, resulting in subsonic combustor conditions. During dual-mode scramjet operation, the precombustion shock train pulls back toward the combustor entrance, resulting in supersonic combustor conditions. Under scramjet operation, the inlet shock continues through the isolator, resulting in supersonic combustor conditions. In the combustor, fuel is injected into the high-speed airflow, whereby mixing creates the conditions for the fuel–air mixture to self ignite and to combust. Finally, the combustion product flow is expanded through the nozzle to allow the flow to accelerate to the ambient speed and to provide a mechanism by which the increase in pressure can be converted into forward thrust. In Fig. 1, the fuel is injected along the engine axis; however, other injection techniques, such as transverse injection, may be used.

Scramjet propulsion research is continuing, but so far only limited success has been reached in building an engine. Part of the reason for the slow pace is the complex nature of the high-temperature reacting flow in the engine. Most research to date has been conducted in ground-based research facilities, but recently, test engines have flown on conventionally powered vehicles. One of the main difficulties in

Received 11 February 2009; revision received 1 June 2009; accepted for publication 10 September 2009.

*Researcher, Defense Security Systems Technology; currently at Scania Group CV AB, SE-151 87 Södertälje, Sweden. Member AIAA.
†Researcher, Defense Security Systems Technology, Grindsjön Research Center.
‡Research Director, Defense Security Systems Technology, Grindsjön Research Center. Senior Member AIAA.
§Leading Scientist, Fundamental and Applied Energetics Department, Chemin de la Huniére.

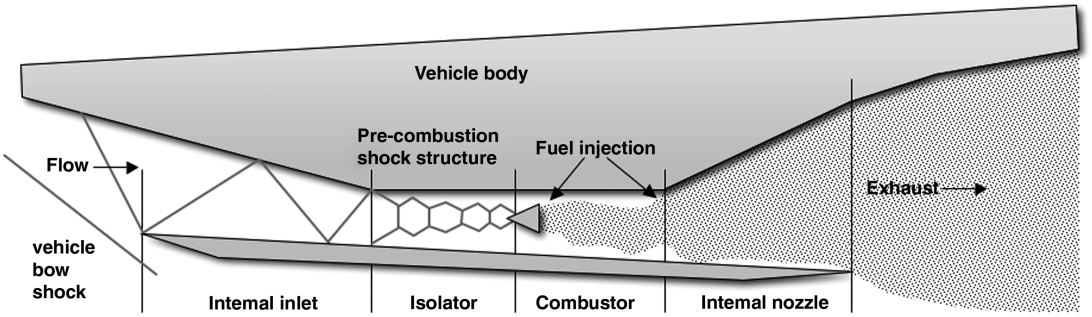

Fig. 1 Schematic of a scramjet engine integrated in a vehicle body.

scramjet progress is the reproduction of its flight conditions. Shock tunnel facilities can make the required conditions, but the test times are often too short. Blowdown facilities generate flow for a longer time, but it is difficult to generate the required conditions (even for $M > 8$) and, usually, the air is contaminated by the combustion products from the air heater. Modeling of scramjet combustion is a formidable task, due to the complex aerothermodynamics. Conventional Reynolds-averaged Navier–Stokes (RANS) models, with simplified combustion models [4], are not detailed enough to predict the convoluted mixing and reaction processes, whereas direct numerical simulation (DNS) is too expensive for practical use. Intermediate large-eddy simulation (LES) models [5,6] have, however, recently been successfully used to investigate supersonic combustion using flamelet models [7] or finite-rate chemistry models [8]. However, to predict (from first principles) the salient features of scramjet combustion, improved reaction mechanisms and turbulence-chemistry interaction models must be incorporated.

The aim of this investigation is to: 1) further validate the finite-rate chemistry LES model against laboratory measurement data [9,10]; 2) study the influence of the reaction mechanism and the turbulence-chemistry interactions in finite-rate chemistry LES; 3) examine the complex flow, mixing, and combustion process in hot vitiated supersonic flow to gain new understanding pertinent to scramjet combustion; and 4) to provide additional general information concerning the use of computational methods (and LES in particular) in scramjet propulsion research. The laboratory facility combines the National Aerospace Laboratory of Japan's (NAL) supersonic combustor [9] (equipped with a two-stage injection strut) and the ONERA/Reactive Flow and Research Techniques Laboratory (LAERTE) air vitiation facility [11], where PLIF and wall pressure measurements of supersonic H_2 combustion have been carried out.

Overview of Large-Eddy Simulation Combustion Modeling

The reactive flow equations are the balance equations of mass, momentum, and energy, describing convection, diffusion, and reactions [4]. In LES, these equations are filtered in order to remove the smallest eddy scales, so that the low-pass filtered equations can be resolved on grids of a manageable size. The filtering introduces additional terms in the filtered equations, representing subgrid mass, momentum, and energy transfer, as well as filtered source terms, such as reaction rates, constitutive equations, and radiative heat loss. Most transfer terms are also found in nonreacting flows, are reasonably well understood, and can be modeled using well-known methods [12,13]. The filtered source terms are specific to reacting flows, and particularly mixing (or species mass transfer) and chemical reactions are closely related (occurring on very small scales), typically resulting in wrinkled interfacial zones, in which most of the reactions take place. This requires specific modeling techniques. Broadly speaking, we differentiate between mixing-based models, flamelet models, and finite-rate chemistry models: all of which may be further subdivided, depending on the assumptions involved in the formulation and modeling [14].

In mixing- based models, the reaction rate is typically described in terms of the variance of the mixture fraction $\tilde{z}''$ (for nonpremixed combustion), the variance of the progress variable $\tilde{c}''$ (for premixed combustion), or the scalar dissipation rate χ, for which transport equations can be formulated and modeled [4] and the tildes denote the low-pass filtering operation performed to eliminate the small (unresolved) scales. These models are usually borrowed from RANS and modified for LES using DNS and experimental data.

In flamelet models, the flame is considered thin when compared with the scales of the flow and, thus, serve as an interface between the fuel and the oxidizer (for nonpremixed combustion) or the reactants and the products (for premixed combustion). Because of separation of scales, the flow modeling is decoupled from the chemistry, which is modeled by the laminar flame speed s_u and by mapping the structure of a one-dimensional (1-D) laminar flame onto the normal of the interface closure is reached. A mixture fraction $\tilde{z}$ is often used for nonpremixed flames, a progress variable $\tilde{c}$ or a kinematic G field is usually used for premixed flames, and, for stratified combustion, both $\tilde{c}$ (or G) and $\tilde{z}$ are required. Turbulence is accounted for by the wrinkling factor Ξ, representing the turbulent wrinkling. LES using flamelet models has been used to analyze scramjet combustion [7], but when the flame is outside of the flamelet regime in the Borghi diagram [4], this approach is no longer useful (due to the interactions between the chemistry and the flow).

The finite-rate chemistry models are based on solving the LES equations for a set of species related by a reduced reaction mechanism $[P_{ij}]\{\Im_i\} = \{0\}$, where P_{ij} is the stoichiometric matrix and $\Im_i$ is the vector of species'. The key issue in this approach is how to incorporate the turbulence-chemistry interactions and the subgrid mixing, as these processes occur at the smallest resolved and subgrid scales. A range of methods and techniques are, however, available that can be used to estimate the filtered reaction rate $\overline{\dot{w}_i}$, including the thickened flame model [15,16] (in which the flame is rescaled to be resolved on the grid while preserving s_u), the probability density function model [17] (in which a transported or a presumed probability density function is used to perform the filtering in composition space), the eddy dissipation concept (EDC) [18] (in which the turbulent cascade process is used to model the reacting volume fraction κ), the partially stirred reactor (PaSR) model [19] (in which κ is estimated as the reacting fraction of the volume swept by the flow structures), and the quasi-laminar (QL) model [20] (in which the subgrid fluctuations are neglected when the filtered reaction rates are evaluated).

Finite-Rate Chemistry Large-Eddy Simulation Model

In this investigation (focusing on self-ignition, mixing, and combustion in hot vitiated air), a finite-rate chemistry model is selected based on the experimental results [9], revealing a distributed flame, well outside of the flamelet regime. In finite-rate chemistry LES, all variables are decomposed into resolved and unresolved (or subgrid) components by a spatial filter, so that $f = \tilde{f} + f''$, where $\tilde{f} = \overline{\rho f}/\bar{\rho}$ is the Favré filtered component and, by filtering the mass, momentum, and energy equations in this way, the reactive LES equations become [4,14,16,21]

$$\begin{cases} \partial_t(\bar{\rho}) + \nabla\cdot(\bar{\rho}\tilde{\mathbf{v}}) = 0 \\ \partial_t(\bar{\rho}\tilde{Y}_i) + \nabla\cdot(\bar{\rho}\tilde{\mathbf{v}}\tilde{Y}_i) = \nabla\cdot(\bar{\mathbf{j}}_i - \mathbf{b}_i) + \overline{\dot{w}_i} \\ \partial_t(\bar{\rho}\tilde{\mathbf{v}}) + \nabla\cdot(\bar{\rho}\tilde{\mathbf{v}}\otimes\tilde{\mathbf{v}}) = -\nabla\bar{p} + \nabla\cdot(\bar{\mathbf{S}} - \mathbf{B}) \\ \partial_t(\bar{\rho}\tilde{E}) + \nabla\cdot(\bar{\rho}\tilde{\mathbf{v}}\tilde{E}) = \nabla\cdot(-\bar{p}\tilde{\mathbf{v}} + \tilde{\mathbf{S}}\tilde{\mathbf{v}} + \bar{\mathbf{h}} - \mathbf{b}_E) + \bar{\rho}\tilde{Q} \end{cases} \tag{1}$$

Here, ρ is the density, $\mathbf{v}$ is the velocity, p is the pressure, $\mathbf{S}$ is the viscous stress tensor, $E = h - p/\rho + \frac{1}{2}\mathbf{v}^2$ is the total energy, h is the enthalpy, $\mathbf{h}$ is the heat flux vector, Y_i is the species mass fraction, $\dot{w}_i$ is the species reaction rate, $\mathbf{j}_i$ is the species mass flux, and Q is the radiative heat loss. The unresolved subgrid physics is concealed in the subgrid stress tensor and flux vectors $\mathbf{B} = \bar{\rho}(\widetilde{\mathbf{v} \otimes \mathbf{v}} - \tilde{\mathbf{v}} \otimes \tilde{\mathbf{v}})$, $\mathbf{b}_i = \bar{\rho}(\widetilde{\mathbf{v}Y_i} - \tilde{\mathbf{v}}\tilde{Y}_i)$, and $\mathbf{b}_E = \bar{\rho}(\widetilde{\mathbf{v}E} - \tilde{\mathbf{v}}\tilde{E})$, which result from filtering the nonlinear terms. Following [20], we assume the gas mixture to be linear, viscous, and optically thin with Fourier heat conduction, Fickian diffusion, and Arrhenius chemistry. We disregard the subgrid contributions to the constitutive equations, so that $\tilde{\mathbf{j}}_i \approx D_i \nabla \tilde{Y}_i$, $\bar{p} \approx \bar{\rho} R \tilde{T} / \Sigma_i (\tilde{Y}_i / M_i)$, $\tilde{\mathbf{S}} \approx 2\mu \tilde{\mathbf{D}}_D$, and $\tilde{\mathbf{h}} \approx \kappa \nabla \tilde{T}$, in which R is the gas constant, M_i is the species molar mass, $\tilde{\mathbf{D}} = \frac{1}{2}(\nabla \tilde{\mathbf{v}} + \nabla \tilde{\mathbf{v}}^T)$ is the rate-of-strain tensor, and $\tilde{\mathbf{D}}_D = \tilde{\mathbf{D}} - \frac{1}{3}\,\mathrm{tr}\tilde{\mathbf{D}}\mathbf{I}$ is its deviatoric part. The viscosity μ is modeled using Sutherland's law, and the species and thermal diffusivities are set to $D_i = \mu / Sc_i$ and $\kappa = \mu / Pr$, respectively, where Sc_i and Pr are the Schmidt and Prandtl numbers. Filtering E in (1_4) results in $\tilde{E} = \tilde{h} - \bar{p}/\bar{\rho} + \frac{1}{2}\tilde{\mathbf{v}}^2 + k$, where $k = \frac{1}{2}(\widetilde{\mathbf{v}^2} - \tilde{\mathbf{v}}^2)$ is the subgrid kinetic energy and

$$\tilde{h} = \Sigma_i (\tilde{Y}_i h_{i,f}^{\theta}) + \Sigma_i \left[\tilde{Y}_i \int_{T_0}^{\tilde{T}} C_{p,i}(T)\, \mathrm{d}T \right]$$

from which the temperature $\tilde{T}$ is obtained. The filtered species reactions rates are $\overline{\dot{w}_i} = M_i \Sigma_{j=1}^{M} P_{ij} \overline{\dot{w}_j}$, in which the reaction rate of the jth reaction step is given by

$$\dot{w}_j = k_{f,j} \Pi_{i=1}^{N} (\rho Y_i)^{P'_{ij}} - k_{b,j} \Pi_{i=1}^{N} (\rho Y_i)^{P''_{ij}}$$

where k_j are the rate constants.

To close the LES equations, we need to provide models for $\mathbf{B}$, $\mathbf{b}_i$, $\mathbf{b}_E$, and $\overline{\dot{w}_i}$, taking the turbulence-chemistry interactions into account. Concerning $\mathbf{B}$, $\mathbf{b}_i$, and $\mathbf{b}_E$, we notice that these terms are not unique to reactive flows and closure models can be acquired from the plethora of subgrid models for nonreactive flows [5]. Here, we employ the mixed model (MM) [13,22], where

$$\mathbf{B} = \bar{\rho}(\tilde{\mathbf{v}} \otimes \widetilde{\tilde{\mathbf{v}}} - \tilde{\tilde{\mathbf{v}}} \otimes \tilde{\tilde{\mathbf{v}}}) - 2\mu_k \tilde{\mathbf{D}}_D$$

$$\mathbf{b}_i = \bar{\rho}(\tilde{\mathbf{v}} \widetilde{\tilde{Y}_i} - \tilde{\tilde{\mathbf{v}}} \widetilde{\tilde{Y}_i}) - \frac{\mu_k}{Sc_t} \nabla \tilde{Y}_i$$

and

$$\mathbf{b}_E = \bar{\rho}(\tilde{\mathbf{v}} \widetilde{\tilde{E}} - \tilde{\tilde{\mathbf{v}}} \tilde{\tilde{E}}) - \frac{\mu_k}{\mathrm{Pr}_t} \nabla \tilde{E}$$

where Sc_t and Pr_t are the turbulent Schmidt and Prandtl numbers $Sc_t = 0.9$ and $Pr_t = 0.7$, respectively, because it better handles the subgrid anisotropy than most eddy viscosity models. The subgrid viscosity, $\mu_k = c_k \bar{\rho} \Delta k^{1/2}$, is obtained from solving a transport equation for the subgrid kinetic energy:

$$\partial_t(\bar{\rho}k) + \nabla \cdot (\bar{\rho}k\tilde{\mathbf{v}}) = -\mathbf{B} \cdot \tilde{\mathbf{D}} + \nabla \cdot (\mu_k \nabla k) - \bar{\rho}\varepsilon$$

where $\varepsilon = c_\varepsilon k^{3/2}/\Delta$ is the subgrid dissipation [22]. The model constants c_k and c_ε are calculated from the classical model of the energy spectra, $\mathcal{E}(\kappa) = C_K \varepsilon^{2/3} \kappa^{-5/3}$, where $C_K \approx 1.50$, by recognizing that

$$k = \int_{\pi/\Delta}^{\infty} \mathcal{E}(\kappa)\, \mathrm{d}\kappa$$

so that $c_k = 0.07$ and $c_\varepsilon = 1.05$. To reduce the computational cost, we use wall-modeled LES, in which a separate subgrid model is used to handle the near-wall flow physics [23]. The model is based on replacing the effective viscosity $(\mu + \mu_k)$ and the thermal and species diffusivities $(\mu/Pr + \mu_k/Pr_t$ and $\mu/Sc_i + \mu_k/Sc_t$, respectively) in the first grid point adjacent to the wall, with values locally derived from the logarithmic law of the wall.

The reaction rate model is required to handle nonunity Lewis number mixing, extinction and reignition, fuel modulation, and different modes of combustion, including accurate predictions of transient species. Mixing-based or flamelet models are unsuitable for this without extensive modifications, hence we focus on a finite-rate chemistry model. Here, we use a PaSR model, adapted for LES [24], with each LES cell being divided into fine structures (denoted by *), in which mixing and reactions are assumed to take place, and surroundings (denoted by ^{0}) are dominated by large-scale coherent flow structures. The conditions in the fine structures and surroundings are coupled by the (subgrid) balance equations of mass, $\bar{\rho}(Y_i^* - Y_i^0)/\tau_m \approx \dot{w}_i(\bar{\rho}, Y_i^*, T^*)$, and energy:

$$\bar{\rho}\Sigma_{i=1}^{N}(Y_i^* h_i^* - Y_i^0 h_i^0)/\tau_m = \Sigma_{i=1}^{N} h_{i,f}^{\theta} \dot{w}_i(\bar{\rho}, Y_i^*, T^*)$$

where τ_m is the subgrid mixing time. By defining the resolved (or filtered) fields (denoted by ~) as $\tilde{Y}_i = \kappa Y_i^* + (1-\kappa)Y_i^0$ and $\tilde{T} = \kappa T^* + (1-\kappa)T^0$, where κ is the reacting volume fraction, the subgrid balance equations become:

$$\begin{cases} \bar{\rho}(Y_i^* - \tilde{Y}_i) = (1-\kappa)\tau_m \dot{w}_i(\bar{\rho}, Y_i^*, T^*) \\ \bar{\rho}\Sigma_{i=1}^{N}[Y_i^* h_i^*(T^*) - \tilde{Y}_i \tilde{h}_i(\tilde{T})] = (1-\kappa)\tau_m \Sigma_{i=1}^{N} h_{i,f}^{\theta} \dot{w}_i(\bar{\rho}, Y_i^*, T^*) \end{cases} \tag{2}$$

To complete the subgrid combustion model, κ and τ_m need to be estimated from the information available to the resolved scales. The smallest scales of relevance to the subgrid mixing are the Kolmogorov scales $\ell_K = (\nu^3/\varepsilon)^{1/4}$, $v_K = (\nu\varepsilon)^{1/4}$, and $\tau_K = (\nu/\varepsilon)^{1/2}$, whereas the largest scales relevant to the subgrid mixing are the subgrid scales $\Delta\ (\geq \ell_K)$, $v' = \sqrt{2k/3}\ (\geq v_K)$, and $\tau' = \Delta/v'$ $(\geq \tau_K)$. As the subgrid mixing occurs on all scales below τ', the subgrid mixing time scale is, here, estimated as the harmonic mean of τ_K and τ', such that $\tau_m = \sqrt{\tau_K \tau'}\ (\geq \tau_K)$. The reacting volume fraction κ is estimated under the assumption of sequential mixing and reaction, each characterized by the time scales τ_m and τ_c, respectively, where the chemical time scale τ_c is estimated as $\tau_c = \delta_u / s_u$, with $\delta_u = \mu/Pr$ as the laminar flame thickness. Hence, κ can be estimated as the ratio between the volume swept by the reacting structures and the volume swept by the mixing and reacting structures, so that $\kappa = \tau_c/(\tau_m + \tau_c)$. The filtered reaction rate $\overline{\dot{w}_i}$ can thus be estimated using κ and the local solution of the subgrid balance Eqs. (2), such that

$$\begin{aligned} \overline{\dot{w}_i(\rho, Y_i, T)} &= \int_{\psi} \wp(\boldsymbol{\psi}) \dot{w}_i(\boldsymbol{\psi})\, \mathrm{d}\boldsymbol{\psi} \approx \kappa \dot{w}_i(\bar{\rho}, Y_i^*, T^*) \\ &+ (1-\kappa)\dot{w}_i(\bar{\rho}, Y_i^0, T^0) \approx \kappa \dot{w}_i(\bar{\rho}, Y_i^*, T^*) \approx \kappa \dot{w}_i(\bar{\rho}, \tilde{Y}_i, \tilde{T}) \end{aligned} \tag{3}$$

where $\wp$ denotes an a priori unknown PDF and $\boldsymbol{\psi} = [\rho, T, Y_k]^T$ is the state space of the PDF. To provide an independent evaluation of the sensitivity of the results to the reaction rate model in Eq. (3), the filtered reaction rates will also be modeled by the QL model, in which the reaction rate is modeled as $\overline{\dot{w}_i} \approx M_i \Sigma_{j=1}^{M} (P''_{ij} - P'_{ij}) \dot{w}_j(\bar{\rho}, \tilde{Y}_i, \tilde{T})$ (i.e., without taking into account the effects of the subgrid turbulence-chemistry interactions). It is sometimes believed that the subgrid turbulence-chemistry interaction model is of critical importance for the success of combustion LES but, as observed in recent studies [25,26] and in the results to be discussed, the choice of model affects the results in some aspects, although it is not of pivotal importance.

Numerical Methods

The code uses an unstructured collocated finite volume (FV) method [27], in which the discretization uses the Gauss theorem together with an explicit time integration scheme. Given the vector of unknown variables, $\bar{\mathbf{u}} = [\bar{\rho}, \bar{\rho}\tilde{Y}_i, \bar{\rho}\tilde{\mathbf{v}}, \bar{\rho}\tilde{E}]^T$, the semidiscretized equations are

$$\partial_t(\bar{\mathbf{u}}_P) + \frac{1}{\delta V_P}\Sigma_f[\mathbf{F}_f^C(\bar{\mathbf{u}}) - \mathbf{F}_f^D(\bar{\mathbf{u}}) + \mathbf{F}_f^B(\mathbf{u}, \bar{\mathbf{u}})] = s_P(\mathbf{u}, \bar{\mathbf{u}}) \quad (4)$$

where $\mathbf{F}_f^C(\bar{\mathbf{u}})$, $\mathbf{F}_f^D(\bar{\mathbf{u}})$, $\mathbf{F}_f^B(\mathbf{u}, \bar{\mathbf{u}})$, and $s_P(\mathbf{u}, \bar{\mathbf{u}})$ are the convective, diffusive, and subgrid fluxes and the source terms, respectively. The flux reconstruction scheme for the convective fluxes, $\mathbf{F}_f^C(\bar{\mathbf{u}})$, is based on hybridizing a high-order linear reconstruction algorithm, $\mathbf{F}_f^{C,H}(\bar{\mathbf{u}})$, with a low-order upwind-biased reconstruction algorithm, $\mathbf{F}_f^{C,L}(\bar{\mathbf{u}})$, using a nonlinear (van Leer) flux limiter, $\Psi(\bar{\mathbf{u}})$, resulting in a total variation diminishing (TVD) convection scheme. To minimize the nonorthogonality errors in the viscous and subgrid fluxes [$\mathbf{F}_f^D(\bar{\mathbf{u}})$ and $\mathbf{F}_f^B(\mathbf{u}, \bar{\mathbf{u}})$, respectively], these are split into orthogonal and nonorthogonal parts. Central difference approximations are applied to the orthogonal part, whereas face interpolation of the gradients of the variables is used for the nonorthogonal parts. The time integration is performed by a second-order accurate TVD Runge–Kutta scheme [28]:

$$\begin{cases} \bar{\mathbf{u}}^* = \bar{\mathbf{u}}^n - \Delta t\left\{\frac{1}{\delta V_P}\Sigma_f[\mathbf{F}_f^C(\bar{\mathbf{u}}^n) - \mathbf{F}_f^D(\bar{\mathbf{u}}^n) + \mathbf{F}_f^B(\mathbf{u}^n, \bar{\mathbf{u}}^n)] - \mathbf{s}_P(\mathbf{u}^n, \bar{\mathbf{u}}^n)\right\} \\ \bar{\mathbf{u}}^{n+1} = \frac{1}{2}(\bar{\mathbf{u}}^n + \bar{\mathbf{u}}^*) - \frac{1}{2}\Delta t\left\{\frac{1}{\delta V_P}\Sigma_f[\mathbf{F}_f^C(\bar{\mathbf{u}}^*) - \mathbf{F}_f^D(\bar{\mathbf{u}}^*) + \mathbf{F}_f^B(\mathbf{u}^*, \bar{\mathbf{u}}^*)] - \mathbf{s}_P(\mathbf{u}^*, \bar{\mathbf{u}}^*)\right\} \end{cases} \quad (5)$$

The equations are solved with full coupling between the equations with a fixed time step corresponding to a Courant number of about 0.4. The discretized equations are investigated using the modified equations analysis [29] to ascertain that the subgrid model does not interact with the leading order truncation error of the numerical method.

The ONERA/Japan Aerospace Exploration Agency Scramjet Experiment

Figure 2a shows a photograph of the experimental supersonic combustion facility, consisting of NALs supersonic combustor [9,10], mounted in the ONERA/LAERTE vitiation air heater [7] and, in Fig. 2b, a schematic of the combustor is shown. The combustor consists of a 0.36 m long constant area duct, with a cross section of 0.05×0.10 m^2, followed by a 0.60 m long diverging area duct, with upper and lower expansion angles of 1.72 deg. For optical access, large quartz windows cover the sides of the combustor. In addition, pressure transducers are arranged along the centerline of the upper wall along the combustor. For the purpose of this investigation, we have chosen to work with the ONH10 two-stage injection strut [9], developed by ONERA and outlined in Fig. 2b. To facilitate ignition and enhance flame stabilization, this injector strut makes use of a first row of $4 \times \phi 2.0$ mm Mach 2.5 injectors (installed on the top and bottom walls of the strut, 27 mm from its base, making a 45 deg angle with the centerline) and a second row of $3 \times \phi 4.3$ mm Mach 2.5 injectors (installed on the strut base, 0.433 m downstream of the combustor entrance). All injector rows have a spacing of 25 mm, with the second-stage injectors located between the rows of the first-stage injectors to improve the fuel–air mixing in the recirculation region. Gaseous H_2, at a temperature of 124 K and a velocity of 2149 m/s, is feed into the $O_2/N_2/H_2O$ mixture with a mass fraction distribution of 0.23:0.70:0.07, at a density of 0.1335 kg/m^3, at a temperature of 830 K, at a velocity of 1449 m/s, and at a pressure of 34.2 kPa. The H_2 mass flow distribution between the first- and second-stage injectors is 40 and 60%, respectively.

To prepare for the LES computations and estimate the flame characteristics, we use the laboratory measurement data to estimate nondimensional key parameters. Based on the velocity and density entering the constant area combustor, the height h of the injection strut, and the viscosity of the vitiated air μ_0, the integral Re number is $Re_I \approx 55,000$. Moreover, by assuming that the integral length scale can be approximated by the height of the injection strut, $\ell_I \approx 0.01$ m, the Kolmogorov and Taylor scales can be estimated as $\ell_K \approx Re_I^{-3/4}h \approx 2.8\ \mu$m and $\ell_T \approx Re_I^{-1/2}h \approx 43\ \mu$m, respectively. Based on the mass flow rates, the global equivalence ratio is $\phi \approx 0.45$, from which the laminar flame speed and flame thickness can be roughly estimated as $s_u = 1.5$ m/s and $\delta_u = 0.1$ mm, respectively, so that $v'/s_u \approx 10$ to 100 and $\ell_I/\delta_u \approx 10$ to 100, respectively. This further implies that $Da = (\ell_I/\delta_u)/(v'/s_u) \approx [0.5, 10]$ and $Ka = (v'/s_u)^{3/2}/(\ell_I/\delta_u)^{1/2} \approx [3, 400]$. In the case of a premixed flame, this would correspond to a thin flame extending into both the distributed reaction regime and the corrugated flame regime, depending on ϕ. Close to the injection strut, intense pocket formation is observed experimentally, hence it is reasonable to believe that the flame here belongs to the distributed regime. Further downstream, the flame changes character and is more similar to a thin or corrugated flame with torn flame fronts and small island formation.

The computational configuration spans the entire combustor (cf. Figure 2), which must be gridded, so that the large-scale coherent flow structures (and as much as possible of the flame) are resolved while maintaining a manageable number of grid cells. Assuming that the grid spacing everywhere would be $2\ell_T$, as is sometimes used as a conservative estimate of the LES grid spacing, this would require about $7.8 \cdot 10^9$ cells: a number far too high for present-day LES. Here, we use an unstructured grid (with finer cells near the walls) in the jet and the injector strut shear layers and around the estimated mean reaction zone, and larger cells are used in between these

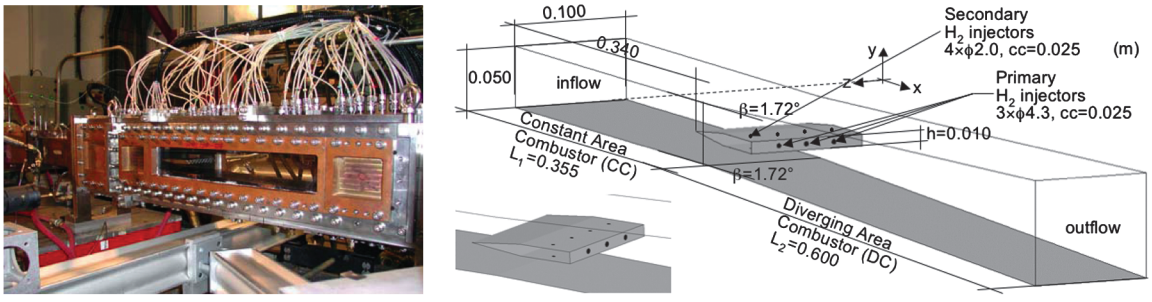

a) b)

Fig. 2 NAL supersonic combustor connected to the ONERA/LAERTE vitiation air heater [7]: a) photograph, and b) schematic [6].

regions, thereby reducing the number of cells. The smallest cell size is $3\ell_T$, being located just downstream of the injector strut, whereas the largest cell size is $20\ell_T$, being located upstream of the injector strut in the constant area combustor. The baseline grid contains ~8.5 million cells , but a coarser grid with ~2.5 million cells and a finer grid with ~17.0 million cells have been constructed to test the grid independence of the first- and second-order statistical moments of **v**, p, T, and Y_i. Dirichlet boundary conditions are used for all variables at the inlet and H_2 injectors. At the outlet, all variables are extrapolated from the interior. At the walls, the no-slip wall model is used together with zero Neumann conditions for all other variables. All runs are initialized with the incoming vitiated air and are left to develop freely for 10 flow-through times, after which a fully developed flow is reached. The runs are continued for an additional 5 to 10 flow-through times (see Table 1), during which the first- and second-order statistical moments of **v**, p, T, and Y_i are sampled.

Combustion Chemistry

Here, we have used three different hydrogen–air reaction mechanisms: the one-step mechanism of Marinov et al. [30], the two-step mechanism of Rogers and Chinitz [31], and the seven-step mechanism of Davidenko et al. [32], with rate parameters according to Table 2. Associated with the reaction mechanism is the treatment of molecular diffusion. Most chemistry packages use polynomial fits for the diffusion coefficients D_k. This technique is accurate, but expensive, and is here replaced by a simpler approximation, assuming that the Schmidt numbers $Sc_k = \mu/D_k$ are constant, so that the diffusion coefficients become $D_k = \mu/Sc_k$, with Sc_k given in Table 3. The thermal diffusivity is modeled similarly with $D_t = \mu/Pr$, where $Pr \approx 0.7$ is the Prandtl number. The unstretched laminar flame speed s_u^0 is obtained from 1-D laminar flame calculations, based on the individual reaction mechanisms. Based on the overall equivalence ratio of $\phi \approx 0.45$ [9], the average unstretched laminar flame speed is 1.5 m/s, resulting in a flame thickness of 100 μm.

To obtain some background information about the reaction mechanisms, they have all been evaluated for constant volume combustion and compared with results from a more detailed 19-step mechanism [33]. Simulations have been performed for a range of pressures p, and for each p, the temperature T was varied between 300 and 2000 K. In Fig. 3a, we compare the mass fraction profiles and the temperature profiles, normalized by the adiabatic flame temperature, between the three reaction mechanisms for an ignition temperature of 700 K and a pressure of 50 kPa. The time t is normalized by the large-eddy turnaround time $\tau_{\text{flow}} = v_0/h \approx 6.9$ μs. For this condition, ignition occurs at about the same time, $0.2\tau_{\text{flow}}$, for all mechanisms, which also gives similar T and Y_i profiles. The two- and seven-step mechanisms are less stiff due to the formation of radicals (OH, O, and H) around the ignition time, thus resulting in a smoother temperature increase. In Fig. 3b, the induction time τ_{ind}, here defined as the time when T has increased by 100 K from the initial state, is presented as a function of T for $p = 50$ kPa for the three mechanisms in Table 2 and for the 19-step reference mechanism [33]. From this, we find that τ_{ind} is well predicted by the seven-step mechanism and reasonably well predicted by the two-step mechanism, whereas the one-step mechanism fails to reproduce the temperature dependence of τ_{ind}. The seven-step mechanism gains its superiority from the chain-branching step $H + O_2 \leftrightarrow OH + O$, the products of which rapidly react with H_2 to produce H, which continues to react (producing even more radicals) until the resulting pool of radicals reaches a critical level, whereby a very rapid exothermic reaction occurs.

Table 3 Schmidt numbers

Species	Sc_i
H_2	0.29
O_2	0.76
H_2O	0.60
OH	0.51
N_2	0.75
O	0.20
H	0.10

Results and Discussion

A first impression of the LES predictions is provided by comparing with spontaneous flame images obtained by a normal video camera [9], as detailed in Fig. 4a. The numerically emulated

Table 1 Summary of the performed ONH10 simulations

Case	Subgrid model	Chemistry	Reaction rate model	Grid cells, million	Sampling time
1	MM	——	——	2.5	4
2	MM	——	——	8.5	4
3	MM	One-step	PaSR	2.5	5
4	MM	Two-step	PaSR	2.5	5
5	MM	Seven-step	PaSR	2.5	5
6	MM	One-step	PaSR	8.5	10
7	MM	Two-step	PaSR	8.5	10
8	MM	Seven-step	PaSR	8.5	10
9	MM	Seven-step	PaSR	17.0	4
10	MM	Seven-step	QL	8.5	8

Table 2 Rate parameters for the different H_2-air mechanisms

Mechanism	No.	Reaction	A [m, kg, mol, s, K]	N	T_a [K]
One-step, [30]	1	$H_2 + 1/2O_2 \rightarrow H_2O$	$5.013 \cdot 10^{13}$	0	17,614
Two-step, [31]	1	$H_2 + O_2 \leftrightarrow OH + OH$	$2.30 \cdot 10^{16}$	0	5,134
	2	$2OH + H_2 \leftrightarrow 2H_2O$	$1.83 \cdot 10^{18}$	0	11,067
Seven-step, [32]	1	$H_2 + O_2 \leftrightarrow OH + OH$	$2.66 \cdot 10^{10}$	0	24,044
	2	$H + O_2 \leftrightarrow OH + O$	$6.21 \cdot 10^{10}$	0	8,456
	3	$OH + H_2 \leftrightarrow H_2O + H$	$3.01 \cdot 10^{6} \cdot T^{1.60}$	1.60	1,660
	4	$O + H_2 \leftrightarrow OH + H$	$1.60 \cdot 10^{3} \cdot T^{2.67}$	2.67	3,163
	5	$OH + OH \leftrightarrow H_2O + O$	$5.21 \cdot 10^{6} \cdot T^{1.14}$	1.14	50
	6	$H + OH + M \leftrightarrow H_2O + M$	$1.30 \cdot 10^{21} \cdot T^{-2.00}$	−2.00	0
	7	$H + H + M \leftrightarrow H_2 + M$	$9.78 \cdot 10^{16} \cdot T^{-0.60}$	−0.60	0

spontaneous flame images are composed of the spanwise-averaged temperature and, in Figs. 4b–4d, the computed emulated spontaneous flame images from cases 6, 7, and 8 are presented. Although not a perfect comparison, it provides some basic insight into the flame dynamics and how the different reaction mechanisms used in the LES mimic the laboratory flame. From the experimental results of Fig. 4a, we note that intensive and quite stable flame emission appears immediately downstream of the strut, with the flame gradually growing in thickness in the wake of the strut until it suddenly widens to a thickness of about 3 h at around $x_{te} \approx 9$ h. This blunt flame front oscillates back and forth, with an amplitude of about 2 to 4 h, and subsequently separate into an upper and lower branch at around $x_{te} \approx 14$ h. The one-step LES of case 6, in Fig. 4b, does not show any such sudden increase in thickness but rather a gradual increase in flame thickness along the whole diverging part of the combustor. Both the two- and seven-step LES of cases 7 and 8 (shown in Figs. 4c and 4d, respectively) initially show a narrow but intense flame that gradually increases in thickness from about h to just above 3 h, between $x_{te} \approx 7$ h and $x_{te} \approx 11$ h, after which time it essentially follows the channel walls throughout the diverging part of the combustor. However, only the seven-step LES of case 8 shows the division into an upper and a lower branch of the flame, originating at around $x_{te} \approx 14$ h, just as in the experimental spontaneous flame images. This suggests that the seven-step LES has potential to capture the processes in the laboratory combustor. Based on the work of George et al. [34], this specific oscillating blunt flame may be a consequence of thermal blockage or supercritical heat release. The one-step mechanism cannot represent this, whereas both the two-step and, in particular, the seven-step mechanisms can capture this feature.

Figure 5 shows perspective views of the combustor flow in terms of isosurfaces of the second invariant of the velocity gradient tensor λ_2 colored by temperature T contours of the vertical gradient of the refraction index $(\nabla n)_y$ at the centerplane (emulating a Schlieren image) and contours of the fuel mass fraction Y_{H2} on a horizontal plane through the injection strut for cases 2, 6, 7, and 8. The index of refraction n is, here, estimated using the Lorenz–Lorentz equation [35] $(n-1)/\rho = c_0(n^2+2)/(n+1) \approx c_G$, in which c_G is the Gladstone–Dale constant. For a mixture of gases, c_G can be estimated as $c_G = \Sigma_{i=1}^{N}(c_{G,i}Y_iM_i)/\bar{M}$ [35], where $\bar{M}$ is the mean molecular weight for the mixture and Y_i, c_{Gi}, and M_i are the species mass fraction, Gladstone–Dale constant, and molecular mass, respectively. For the nonreacting case 2 (Fig. 5a), oblique shocks appear at the leading edge of the strut, reflecting first in the combustor wall, then in the strut, and again in the combustor wall before striking the unsteady inhomogeneous H_2-filled wake. Together with the weakly bent expansion fans, coming off the trailing edges of the injection strut, this causes a distinctive shock wave pattern to develop further downstream in the diverging area combustor. At the walls, the boundary layer thickens, and the temperature and pressure fluctuations increase as a result of the shock boundary layer interactions. The strut boundary layers separate at the base to develop parallel unstable shear layers that break up and develop Kelvin–Helmholtz (KH) vortices, which initially are in phase with each other.

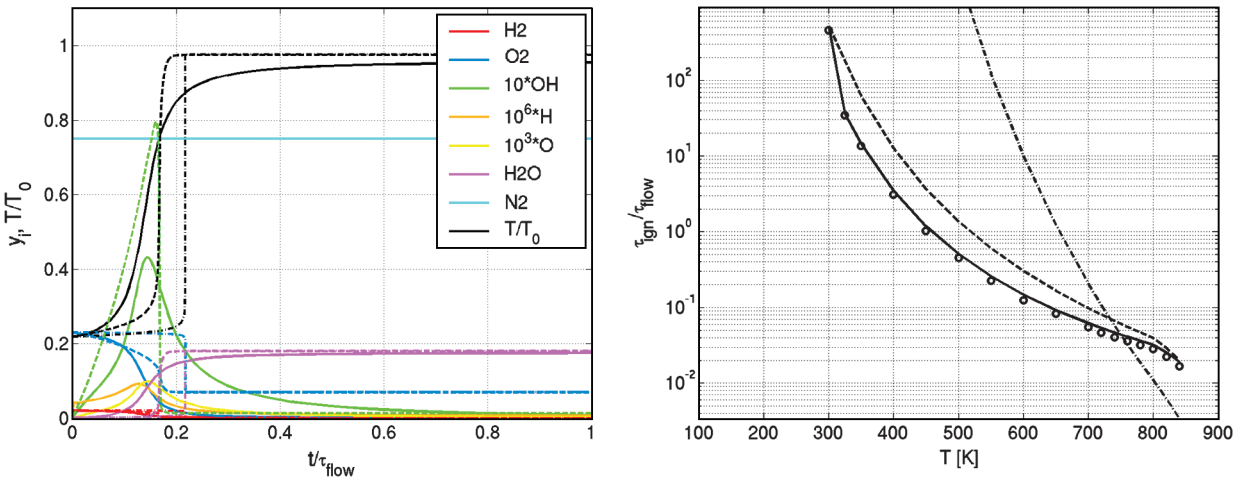

Fig. 3 Different H_2-air mechanisms (from Table 2): a) mass fraction and temperature profiles vs normalized time for an ignition temperature of 700 K and a pressure of 100 kPa; and b) ignition delay time chart. [One-step mechanism (dash dot), two-step mechanism (dash), seven-step mechanism (solid line), and 19-step reference (circles).]

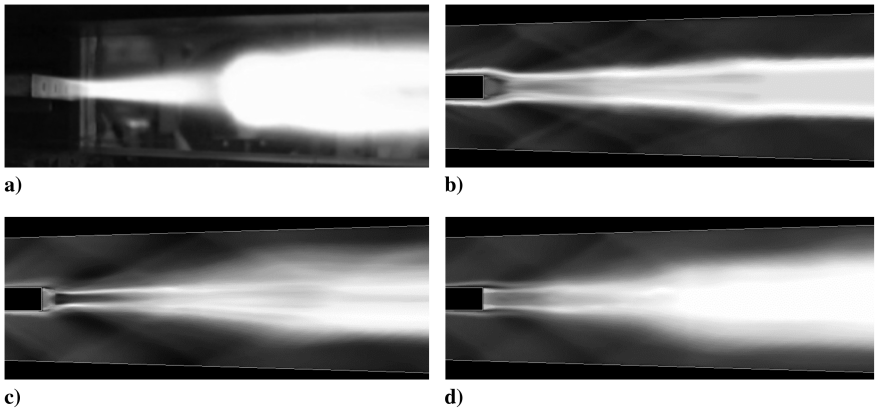

Fig. 4 Comparison of instantaneous spontaneous flame images obtained: a) experimentally by a normal video camera and numerically from the spanwise-averaged temperature from b) the one-step LES of case 6, c) the two-step LES of case 7, and d) the seven-step LES of case 8.

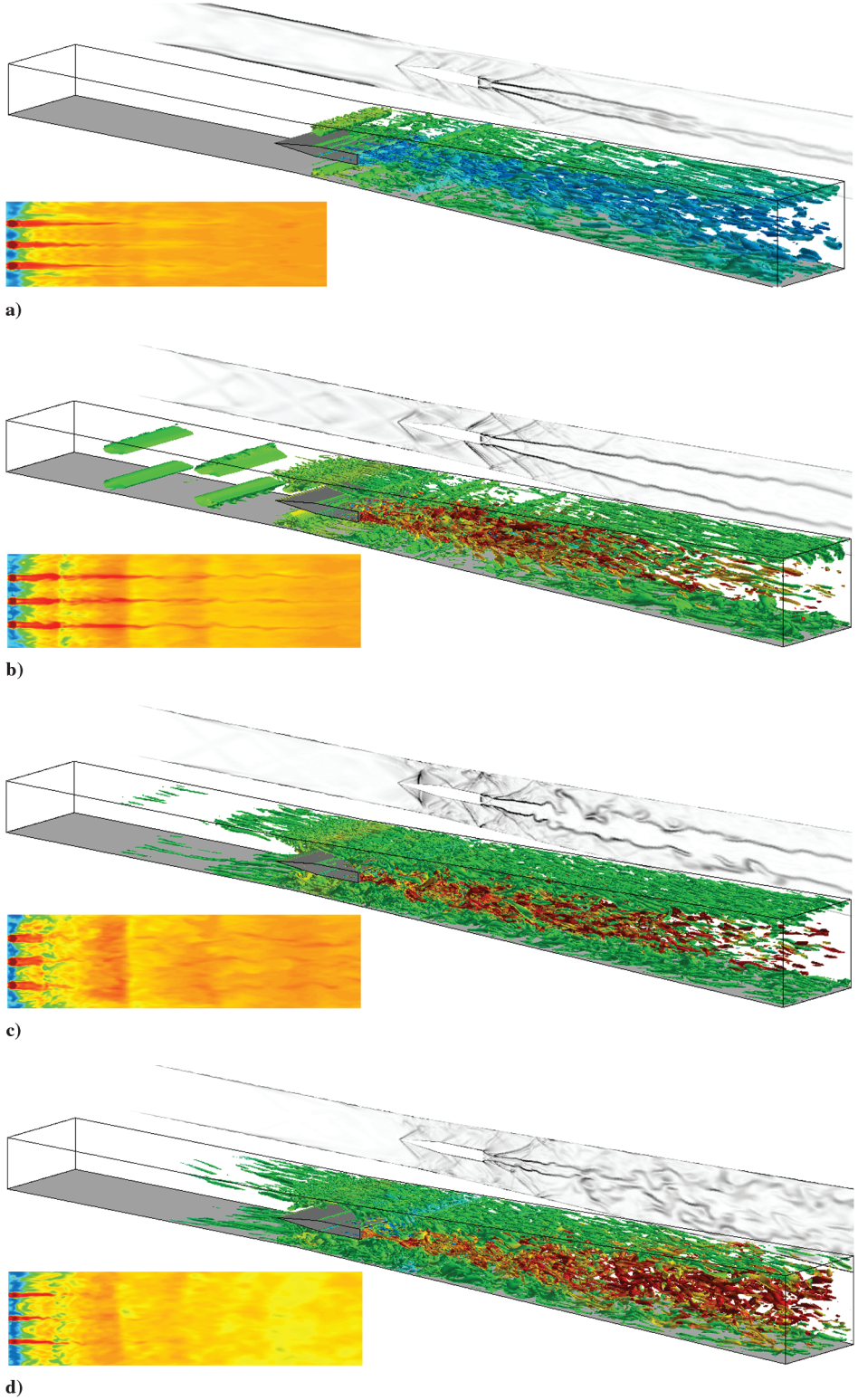

Fig. 5 Perspective views of the combustor flow in terms of isosurfaces of the second invariant of the velocity gradient tensor λ_2 colored by temperature T contours of the vertical gradient of the refraction index $(\nabla n)_y$ at the centerplane, emulating a Schlieren image, and contours of the axial velocity v_x on a horizontal plane through the injection strut for cases 2, 6, 7, and 8, respectively.

Because of the small strut height, these rapidly start to interact and, due to vortex stretching and baroclinic torque effects, the shear layers become gradually entwined, forming a complex wake. Both grids (cases 1 and 2) are able to capture this complicated shock-vortex dynamics, but the finer grid reveals more details. The wake development is assisted by the primary H_2 jets injecting high-momentum H_2-rich fluid into the wake and by the secondary H_2 jets injecting low-momentum H_2-rich fluid into the vitiated flow passing above and below the injection strut, which subsequently becomes entrained into the wake.

Figures 5b–5d present similar perspective views from the one-, two- and seven-step reacting cases 6, 7, and 8, respectively. The key features of these cases are similar but with important differences due to the intrinsic features of the reaction mechanisms, as will be discussed later. With combustion, the recirculation region behind the strut becomes longer and wider and stabilizes the flame. As a result of

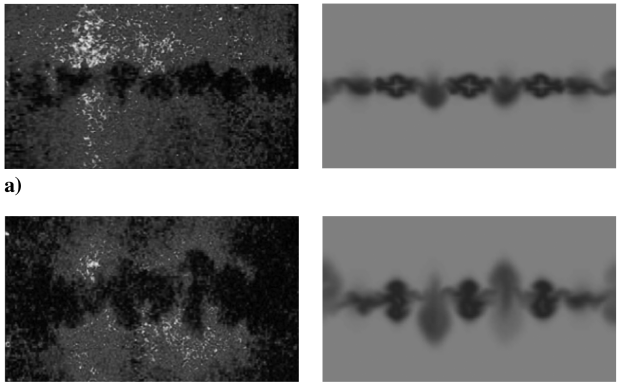

Fig. 6 Comparison of measured [9] OH-PLIF images with predicted short time-averaged Y_{H2} mass fraction distributions from case 2 at: a) $x_{te} = 4$ h and b) $x_{te} = 10$ h.

the exothermicity, the strut base pressure increases, as compared with the inert case, and the shear layers that shed off the trailing strut edges become more pronounced, because ignition occurs intermittently between the inhomogeneous H_2-rich wake and the ambient flow. The flow can be divided into three regions: the induction zone (where turbulence controls the mixing and combustion and the flame essentially follows the shear layers), the transitional zone that is dominated by large-scale coherent structures, convective mixing, and exothermicity (where the flame escapes the shear layers to develop three-dimensional (3-D) undulating structures), and the turbulent combustion zone, governed by large-scale coherent structures and mixing (where the flame finally develops a strong 3-D undulating pattern). As for the inert H_2-injection case, the KH vortices originate in the shear layers that roll up and become increasingly distorted with downstream distance, due to vortex breakdown, baroclinic torque effects, shock reflections, exothermicity, and delayed mixing. Longitudinal vortices develop between the KH vortices but are wider than for the inert H_2-injection case, due to the temperature-dependent viscosity that also aids in stabilizing the flow. Exothermicity increases the shear layer thickness, which, in turn, influences the reflections of the oblique shocks and the pressure. The flames from all three mechanisms are found to attach to the base of the strut and widen throughout the induction zone, after which the flame becomes thicker. As evident from the Schlieren images, but also from the Y_{H2} and λ_2 fields, the flow in the diverging combustor becomes more convoluted with the increasing complexity of the chemical reaction mechanism. For the one-step mechanism, the induction time τ_{ind} is much shorter than the time scales of the flow (i.e., $\tau_{ind} < \tau_{flow}$), corresponding to a corrugatedlike flame that does not easily interact with the vortical structures and discontinuities in the combustor. For the two- and seven-step mechanisms, τ_{ind} is on the order of τ_{flow}, such that $\tau_{ind} \approx \tau_{flow}$, which then indicate the vortices interacting with and wrinkling the flame. The differences between the two- and seven-step mechanism predictions are less pronounced than the differences between the one- and two- step mechanisms and are due primarily to the convective transport and differential and preferential diffusions of O and H, resulting in an even larger exothermally active volume, which, due to the turbulent transport processes, is geometrically very convoluted.

In Fig. 6, we compare measured and predicted planar laser-induced fluorescence imaging of hydroxide–ion radicals (OH-PLIF) distributions, originally contained within the freestream vitiated air, with Y_{H2} (appearing as dark regions) for case 2 at 4 and 10 h downstream of the strut base. The computed OH distribution is averaged over 50 time steps to emulate the intensifier gate width of 500 ns. In the LES results, the primary and secondary fuel jets are visible at $x_{te} = 4$ h, whereas at $x_{te} = 10$ h, they have merged to form a characteristic pattern. From the measurements, similar distributions are observed, and the downstream evolution of the fuel jets is well predicted by the LES. Moreover, the width of the H_2-rich wake evolves from ∼h to ∼1.4 h, between $x = 4$ and 10 h, in both the LES and the measurement data, suggesting that the mixing is well modeled by the LES.

In Fig. 7, we compare measured and predicted OH-PLIF distributions after ignition at $x_{te} = 4$ and 10 h, downstream of the strut base. The computed OH distribution is averaged over 50 time steps to match the intensifier gate width of 500 ns. For the one-step LES, Y_{OH} is modeled from the equilibrium conditions for OH formation:

$$Y_{OH} = \frac{M_{OH}}{M_{O2}^{1/2} M_{H2}^{1/2}} (k_C^1 k_C^2 Y_{O2} Y_{H2})^{1/2}$$

where k_C^1 and k_C^2 are the equilibrium constants for $H + O_2 \leftrightarrow OH + O$ and $O + H_2 \leftrightarrow OH + H$, respectively. At $x_{te} = 4$ h, the experimental data show high levels of OH between the second-stage fuel jets, suggesting that ignition and subsequent combustion occurs early, using fuel mainly from the first-stage injectors. In the one- and two-step LES (cases 6 and 7), higher levels of OH are found in thin structures enveloping both the first- and second-stage injector jets, suggesting too-early ignition, combustion, and lack of fuel–air mixing. In the seven-step LES (case 8), high levels of OH are found between the second-stage fuel jets that are in good qualitative and

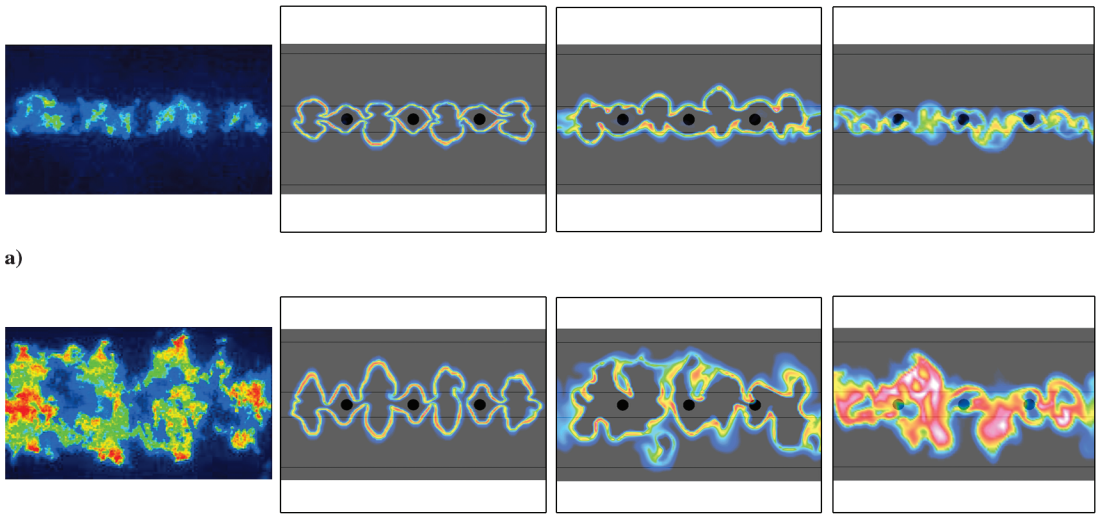

Fig. 7 Comparison of OH-PLIF images from [9] (far left) with predicted short time-averaged Y_{OH} mass fraction distributions from cases 6 (second from left), 7 (third from left), and 8 (far right), respectively, at: a) $x_{te} = 4$ h and b) $x_{te} = 10$ h. Note that the scale is the same for all computational cases 6, 7, and 8 and corresponds to that of the experiments.

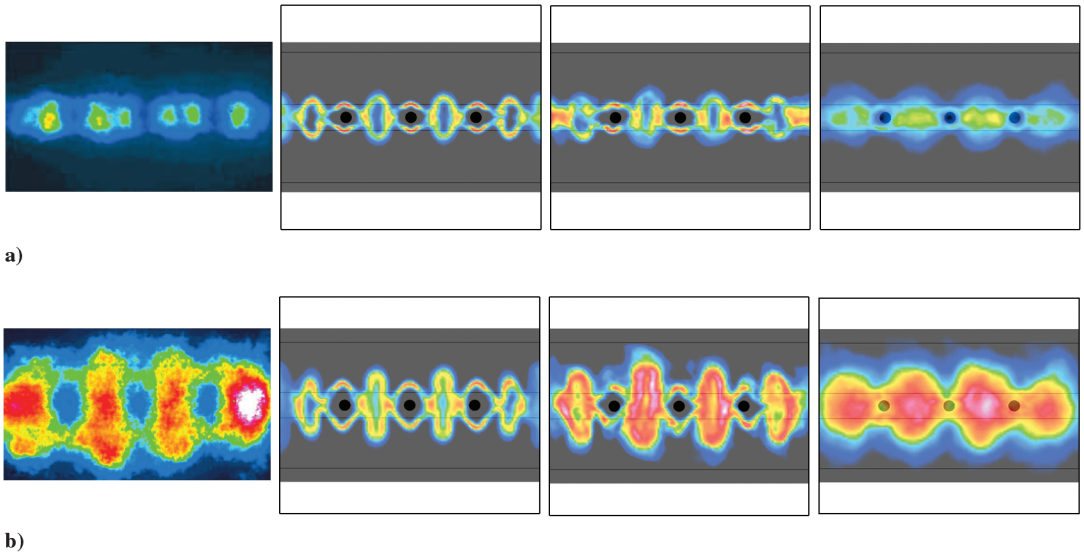

Fig. 8 Comparison of mean OH-PLIF images from [9] (far left) with predicted long time-averaged $\langle Y_{OH} \rangle$ mass fraction distributions from cases 6 (second from left), 7 (third from left), and 8 (far right), respectively, at: a) $x_{te} = 4$ h and b) $x_{te} = 10$ h. Note that the scale is the same for all computational cases 6, 7, and 8 and corresponds to that of the experiments.

quantitative agreements with the experiments. In case 8, ignition is also found to occur at the outer edge of the second-stage fuel jets and appears stable (as supported by the experimental data). Comparing Figs. 6 and 7, we find that the vertical extents of the structures are larger for the reacting cases, revealing the effects of volumetric expansion due to exothermicity. At $x_{te} = 10$ h, the experimental data show high levels of OH in large volumes around the second-stage fuel jets and low OH levels in the core of each jet, indicating that these are fairly coherent. For the one- and two-step LES (cases 6 and 7), OH continues to occur in thin structures enveloping both the first- and second-stage fuel injector jets, whereas for the seven-step LES (case 8), OH is found in thick complex-shaped structures surrounding the second-stage fuel injector jets and wrinkled by the vorticity field (cf. Fig. 5d), being in good qualitative and quantitative agreements with the measured OH distributions.

In Fig. 8, we compare time-averaged, measured, and predicted OH-PLIF distributions after ignition at $x_{te} = 4$ and 10 h, downstream of the strut base. The computed OH distribution is averaged over 10 flow-through times to match the experimental averaging procedure [9] using 30 to 50 instantaneous images, with images of poor combustion due to blow off removed. At $x_{te} = 4$ h, the best agreement is obtained for the seven-step mechanism, as expected from the instantaneous OH comparisons of Fig. 7a, but with the results of the two-step mechanism also showing acceptable agreement, with the exception of the high $\langle \tilde{Y}_{OH} \rangle$ values above and below the second-stage injector jets. At $x_{te} = 10$ h, the best agreement is also obtained for the seven-step mechanism, as anticipated from the instantaneous OH comparisons of Fig. 7b, but once more with the results of the two-step mechanism showing acceptable qualitative and quantitative agreements.

Based on Figs. 7 and 8, it appears as if the difference in ignition delay time between the one- and two-step mechanisms, on the one hand, and the seven-step mechanism, on the other hand, is sufficient to allow large-scale convective transport of intermediate species (O, H and OH) and mixing to occur, taking the species-specific Sc numbers into account. For the seven-step mechanism and, to a limited extent, the two-step mechanism, these transport processes lead to local accumulation of the intermediate species in complex-shaped pockets between the large-scale coherent vortical structures, as shown in Fig. 5. In these pockets, small-scale mixing dominates over large-scale vortical mixing, creating the proper conditions for continued reactions. Once these conditions are reached, the combustion taking place is very fast, thus rapidly releasing large amounts of energy and affecting the surrounding vortical flow through volumetric expansion ($\nabla \cdot \tilde{\mathbf{v}}$ in the continuity equation), raising the pressure, exothermicity ($\tilde{T} \nabla \tilde{s} - \nabla \tilde{h}$, where s is the entropy, in the equation for the kinetic energy), and accelerating the flow. For the seven-step mechanism, the chain-branching step $H + O_2 \leftrightarrow OH + O$ is particularly important, as its products react with H_2 to produce H, which in turn reacts again to produce H, O, and OH, accumulating in the pockets.

Figure 9a presents the instantaneous pressure distributions on the upper and lower walls, and on the centerplane in case 8, together with an isosurface of temperature colored by the pressure. Based on Figs. 5 and 9a, the wedge shock and its reflections on the combustor walls, as well as on the injection strut, can clearly be seen together with the slightly bent expansion fan coming off the base of the injection strut and the bow shocks around the secondary injectors. In the diverging part of the combustor, the reflections of the pressure waves on both the combustor walls and on the temperature isosurface (representing the flame) can be noticed. Quantitative comparisons between measured and predicted wall pressures along the lower combustor wall are presented in Figs. 9b and 9c for a nonreacting situation, corresponding to cases 1 and 2, and a reacting situation, corresponding to cases 6, 7, 8, and 10. For the inert H_2 injection cases 1 and 2 (Fig. 9b), reasonable agreement is obtained between the LES and the measurement data, and only marginal differences are observed between the coarse and fine-grid predictions. The predicted pressure upstream of the injector is higher than the measured, which may be caused by a too-large viscous drag, whereas the increase in wall pressure toward the end of the combustor is likely to be caused by facility details not included in the computational model. The peak wall pressure is observed downstream of the strut leading edge, due to the incidence of the shock wave emanating from the strut leading edge (interacting with the wall boundary layer), and the leading edge shock causes separation of the wall boundary layer upstream of its incident location. For the combusting cases 6, 7, 8, 9, and 10 (Fig. 9c), this separation virtually disappears, and the pressure increases downstream of the injection strut due to the volumetric expansion. Figure 9c indicates that the agreement with the experimental data improves slightly with increasing grid resolution and considerably with inclusion of more realistic chemistry, whereas the influence of the subgrid combustion model is virtually negligible. This is consistent with the results of other studies [34,36]. The differences between the seven-step LES and the measurement data may be explained by a too-short sampling time, and it has been reported [36] that 35 residence times may be needed to predict this mode (characterized by large subsonic zones) of combustion, as illustrated in the Mach number contours in Fig. 9a. Another key issue may be too-slow mixing in comparison with the time of combustion.

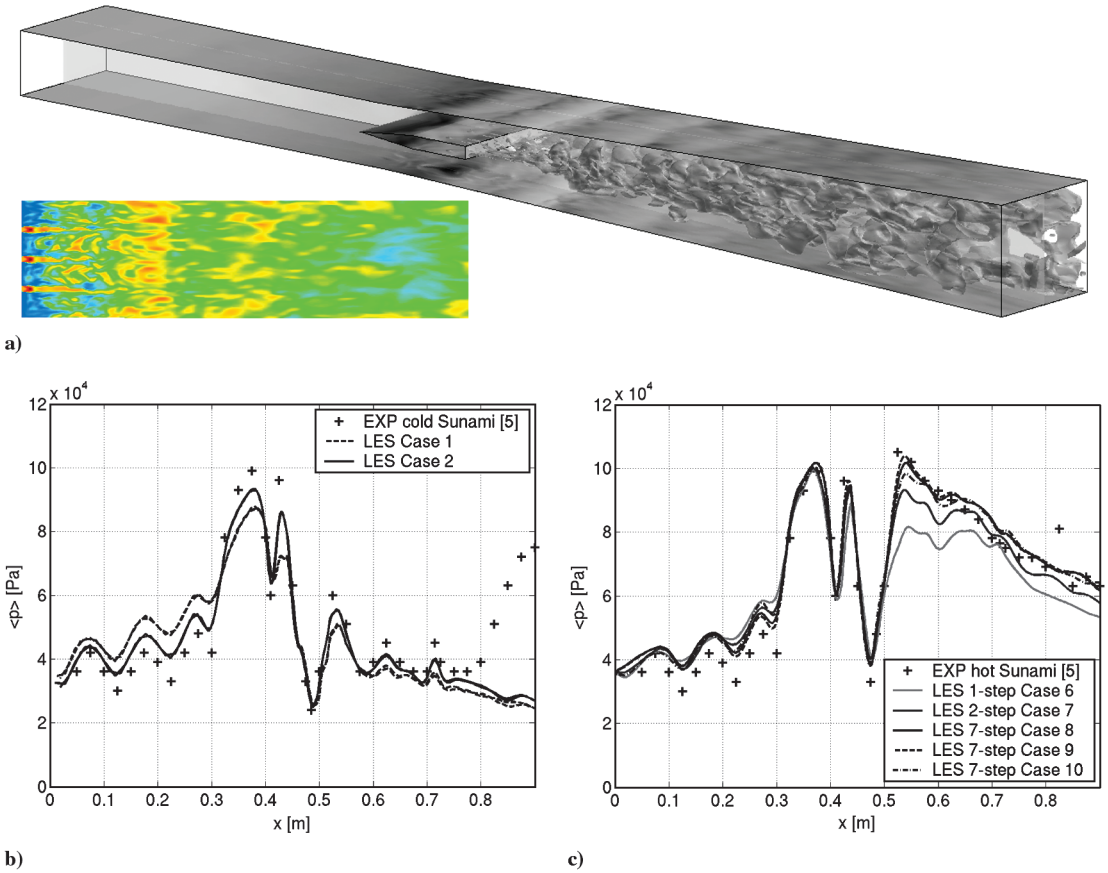

Fig. 9 Comparison of pressure: a) perspective view on the pressure distributions on the upper and lower walls and on the centerplane and an isosurface of the temperature at $T = 1400$ K, together with contours of the Mach number ($0 < M < 3$) on a horizontal plane through the injection strut, and time-averaged wall pressure distributions along the lower combustor wall for: b) inert H2 injection and c) combustion.

For the one- and two-step LES, the combustion efficiency η at $x_{te} = 60$ h is 71 and 73%, respectively, and for the seven-step LES, $\eta \approx 95\%$, indicating the need for detailed chemistry and the importance of differential and preferential species diffusion and its influence on the reactions.

Conclusions

In this study, LES has been applied to a joint French–Japanese laboratory scramjet combustor to examine the influence of finite-rate chemistry and to enhance our understanding of supersonic combustion. An explicit PaSR finite-rate chemistry LES model is used together with one-, two-, and seven-step reaction mechanisms. A second-order accurate unstructured FV discretization is used to discretize the LES equations. The induction times of these mechanisms are compared with a 19-step mechanism, resulting in good agreement for the seven-step mechanism and reasonable agreement for the two-step mechanism. For the scramjet LES, two grids of 2.5 and 8.5 million cells are used and, although more details are found in the fine-grid LES, the large-scale flow features are also resolved on the coarse grid. In the combustor, the flame is anchored in the wake of the two-stage wedge-shaped injection struts. The combustion region can be divided into an induction zone (in which the flame essentially follows the shear layers), the transitional zone (in which the flame escapes the shear layers to develop 3-D structures), and the turbulent combustion zone (in which the flame finally develops a strong 3-D undulating pattern). Comparison between predicted and measured wall pressure and OH-PLIF distributions suggests that, although all LES captures the gross features, the seven-step LES is the only model that can match the wall pressure amplitudes and the OH distributions. The reason for this is that the seven-step LES allows transport and convective mixing of O, H, and OH, as well as appropriate reaction kinetics.

Acknowledgments

This work was supported by the Swedish Defense Material Agency, with E. Prisell serving as project officer. T. Sunami is acknowledged for providing the experimental data, and we also acknowledge P. Magre for valuable support and discussions.

References

[1] Fry, R. S., "A Century of Ramjet Propulsion Technology Evaluation," *Journal of Propulsion and Power*, Vol. 20, No. 1, 2004, pp. 27–58. doi:10.2514/1.9178

[2] Curran, E. T., "Scramjet Engines: The First Forty Years," *Journal of Propulsion and Power*, Vol. 17, No. 6, 2001, pp. 1138–1148. doi:10.2514/2.5875

[3] Andreadis, D., "Scramjets Integrate Air and Space," *Industrial Physicist*, Vol. 10, No. 4, Aug.–Sept. 2007, pp. 24–27.

[4] Poinsot, T., and Veynante, D., *Theoretical and Numerical Combustion*, R. T. Edwards, Philadelphia, 2001.

[5] Sagaut, P., *Large Eddy Simulation for Incompressible Flows*, Springer–Verlag, Heidelberg, 2001.

[6] Grinstein, F. F., Margolin, L., and Rider, B., *Implicit Large Eddy Simulation: Computing Turbulent Fluid Dynamics*, Cambridge Univ. Press, New York, 2007.

[7] Berglund, M., and Fureby, C., "LES of Supersonic Combustion in a Scramjet Engine Model," *Proceedings of the Combustion Institute*, Vol. 31, No. 2, Jan. 2007, pp. 2497–2504. doi:10.1016/j.proci.2006.07.074

[8] Génin, F., Chernyavsky, B., and Menon, S., "Large Eddy Simulation of Scramjet Combustion using a Subgrid Mixing/Combustion Model," AIAA Paper 03-7035, 2003.

[9] Sunami, T., Magré, P., Bresson, A., Grisch, F., Orain, M., and Kodera, M., "Experimental Study of Strut Injectors in a Supersonic Combustor using OH-PLIF," AIAA Paper 2005-3304, 2005.

[10] Sunami, T., Murakami, A., Kudo, K., Kodera, M., and Nishioka, M., "Mixing and Combustion Control Strategies for Efficient Scramjet

Operation in Wide Range of Flight Mach Numbers," AIAA Paper 2002-5116, 2002.

[11] Collin, G., Dessornes, O., and Magre, P., "Installations D'essais pour les Recherches Fondamentales en Propulsion," Communications to PEP/FDP AGARD on Aerospace Technology in the Service of the Alliance, Office National d'Etudes et de Recherches Aerospatiales Rept. ONERA-TAP-97-32, Palaiseau, France, 1997.

[12] Temmerman, L., Leschziner, M. A., Mellen, C. P., and Fröhlich, J., "Investigation of Wall Function Approximations and Subgrid Scale Models in Large Eddy Simulation of Separated Flow in a Channel with Streamwise Periodic Constrictions," *International Journal of Heat and Fluid Flow*, Vol. 24, No. 2, 2003, pp. 157–180. doi:10.1016/S0142-727X(02)00222-9

[13] Bensow, R. E., and Fureby, C., "On the Justification and Extension of Mixed Models in LES," *Journal of Turbulence*, Vol. 8, No. 54, 2007, pp. 1–17. doi:10.1080/14685240701742335

[14] Fureby, C., "Comparison of Flamelet and Finite Rate Chemistry LES for Premixed Turbulent Combustion," AIAA Paper 2007-1413, 2007.

[15] O'Rourke, P. J., and Bracco, F. V., "Two Scaling Transformations for the Numerical Computation of Multidimensional Unsteady Laminar Flames," *Journal of Computational Physics*, Vol. 33, No. 2, 1979, pp. 185–203. doi:10.1016/0021-9991(79)90015-9

[16] Colin, O., Ducros, F., Veynante, D., and Poinsot, T., "A Thickened Flame Model for Large Eddy Simulations of Turbulent Premixed Combustion," *Physics of Fluids*, Vol. 12, No. 7, 2000, pp. 1843–1863. doi:10.1063/1.870436

[17] Girimajii, S. S., "Assumed β-PDF Model for Turbulent Mixing: Validation and Extension to Multiple Scalar Mixing," *Combustion Science and Technology*, Vol. 78, Nos. 4–6, 1991, pp. 177–196. doi:10.1080/00102209108951748

[18] Ertesvåg, I. S., and Magnussen, B. F., "The Eddy Dissipation Turbulence Energy Cascade Model," *Combustion Science and Technology*, Vol. 159, No. 1, 2000, pp. 213–235. doi:10.1080/00102200008935784

[19] Karlsson, J. A. J., "Modeling Auto-Ignition, Flame Propagation and Combustion in Non-Stationary Turbulent Sprays," Ph.D. Thesis, Chalmers Univ. of Technology, Göteborg, Sweden, 1995.

[20] Grinstein, F. F., and Kailasanath, K. K., "Three Dimensional Numerical Simulations of Unsteady Reactive Square Jets," *Combustion and Flame*, Vol. 100, Nos. 1–2, 1995, pp. 2–10. doi:10.1016/0010-2180(94)00095-A

[21] Génin, F., Chernyavsky, B., and Menon, S., "Large Eddy Simulation of Scramjet Combustion Using a Subgrid Mixing/Combustion Model," AIAA Paper 03-7035, 2003.

[22] Speziale, C. G., Erlebasher, G., Zang, T. A., and Hussaini, M. Y., "The Subgrid Scale Modeling of Compressible Turbulence," *Physics of Fluids*, Vol. 31, No. 4, 1988, pp. 940–942. doi:10.1063/1.866778

[23] Fureby, C., "On LES and DES of Wall Bounded Flows," *ERCOFTAC Bulletin* , Vol. 72, March 2007.

[24] Baudoin, E., Nogenmyr, K. J., Bai, X. S., and Fureby, C., "Comparison of LES Models Applied to a Bluff Body Stabilized Flame," AIAA Paper 2009-1178, 2009.

[25] Fureby, C., "Comparison of Flamelet and Finite Rate Chemistry LES for Premixed Turbulent Combustion," AIAA Paper 2007-1413, 2007.

[26] Nogenmyr, K.-J., Fureby, C., Bai, X. S., Petersson, P., and Linné, M., "Large Eddy Simulation and Laser Diagnostic Studies on a Low Swirl Stratified Premixed Flame," *Combustion and Flame*, Vol. 156, No. 1, 2009, pp. 25–36.

[27] Weller, H. G., Tabor, G., Jasak, H., and Fureby, C., "A Tensorial Approach to CFD Using Object Oriented Techniques," *Computers in Physics*, Vol. 12, No. 6, 1998, pp 620–631. doi:10.1063/1.168744

[28] Gottlieb, S., and Shu, C.-W., "Total Variational Diminishing Runge–Kutta Schemes," *Mathematics of Computation*, Vol. 67, No. 221, 1998, pp. 73–85. doi:10.1090/S0025-5718-98-00913-2

[29] Drikakis, D., Fureby, C., Grinstein, F. F., and Liefendahl, M., "ILES with Limiting Algorithms," *Implicit Large Eddy Simulation: Computing Turbulent Fluid Dynamics*, edited by F. F. Grinstein, L. Margolin, and B. Rider, Cambridge Univ. Press, Cambridge, England, U.K., 2007, pp. 94–129.

[30] Marinov, N. M., Westbrook, C. K., and Pitz, W. J., "Detailed and Global Chemical Kinetics Model for Hydrogen," *Transport Phenomena in Combustion*, edited by S. H. Chan, Vol. 1, Taylor and Frances, Washington, D.C., 1996.

[31] Rogers, R. C., and Chinitz, W., "On the Use of Hydrogen–Air Combustion Model in the Calculation of Turbulent Reacting Flows," AIAA Paper 1982-0112, 1982.

[32] Davidenko, D. M., Gökalp, I., Dufour, E., and Magre, P., "Systematic Numerical Study of the Supersonic Combustion in an Experimental Combustion Chamber," AIAA Paper 06-7915, 2006.

[33] Mauss, F., Peters, N., Rogg, B., and Williams, F. A., "Reduced Kinetic Mechanisms for Premixed Hydrogen Flames," *Reduced Kinetic Mechanisms for Application in Combustion Systems*, Lecture Notes in Physics, edited by N. Peters and B. Rogg, Springer–Verlag, New York, 1993, p. 29. doi:10.1007/978-3-540-47543-9

[34] George, E., Sabelnikov, V., and Magré, P., "Self-Ignition of Ethylen-Hydrogen Mixtures in Unsteady Thermal Choking Conditions: Numerical Unsteady RANS Investigations," *West-East High Speed Flow Field Conference*, European Community on Computational Methods in Applied Sciences, Barcelona, 19–22 Nov. 2007, pp. 1–11.

[35] Vasilev, L. A., *Schlieren Methods*, Jerusalem, Israel Program, Keter, New York., 1971.

[36] George, E., Sabel'nikov, V., and Magre, P., "LES and Experimental Study of Self-Ignition of Supersonic Hydrogen and Methane-Hydrogen Jets in a Vitiated Confined Supersonic Air Stream," *Proceedings of the 5th International Symposium on Turbulence and Shear Flow Phenomena*, edited by Friedrich, R., Adams, N. A., Eaton, J. K., Humphrey, J. A. C., Kasagi, N., and Leschziner, M. A., Vol. 3, Technical Univ. of Munich, Munich, 2007, pp. 1009–1014.

F. Ladeinde
Associate Editor